




Analytical model of the acoustic response of nanogranular films adhering to a substrateGianluca Rizzi ¹, Giulio Benetti ^{2,*}, Claudio Giannetti ³, Luca Gavioli ^{3,4} and Francesco Banfi ⁴¹GEOMAS, INSA-Lyon, Université de Lyon, 20 avenue Albert Einstein, 69621, Villeurbanne cedex, France²Department of Pathology and Diagnostics-Medical Physics Unit, University Hospital of Verona, P.le Stefani 1, 37126 Verona, Italy³Interdisciplinary Laboratories for Advanced Materials Physics (I-LAMP) and Dipartimento di Matematica e Fisica, Università Cattolica del Sacro Cuore, Via Musei 41, 25121 Brescia, Italy⁴FemtoNanoOptics group, Université de Lyon, CNRS, Université Claude Bernard Lyon 1, Institut Lumière Matière, F-69622 Villeurbanne, France

(Received 25 January 2021; revised 7 June 2021; accepted 10 June 2021; published 12 July 2021)

A one-dimensional (1D) mechanical model for nanogranular films, based on a structural interface, is presented. The analytical dispersion relation for the frequency and lifetimes of the acoustics breathing modes is obtained in terms of the interface layer thickness and porosity. The model is successfully benchmarked both against three-dimensional finite element method simulations and experimental photoacoustic data on a paradigmatic system available from the literature. A simpler 1D model, based on an homogenized interface, is also presented and its limitations and pitfalls discussed at the light of the more sophisticated pillar model. The pillar model captures the relevant physics responsible for acoustic dissipation at a disordered interface. Furthermore, the present findings furnish to the experimentalist an easy-to-adopt, benchmarked analytical tool to extract the interface layer physical parameters upon fitting of the acoustic data. The model is scale invariant and may be deployed, other than the case of granular materials, where a patched interface is involved.

DOI: [10.1103/PhysRevB.104.035416](https://doi.org/10.1103/PhysRevB.104.035416)**I. INTRODUCTION**

Nanogranular ultrathin films are at the forefront of a wide range of technological applications [1] ranging from nanomedicine [2], sensing [3–5], to electronics [6–12]. Accessing their mechanical properties, both within the film's bulk and at the interface region in contact with the supporting substrate, is among the most urgent issues in view of any device development. In this context photoacoustic nanometrology plays a key role. For instance, the bulk properties of periodic nanogranular thin films have been explored across a variety of configurations [13,14] ranging from 1D [15], two-dimensional (2D) [16–22], to three-dimensional (3D) [23,24] arrangements. Recently, the development of table-top UV laser sources allowed generating surface acoustic waves with periodicity in the 10 nm range [25], hence opening to mechanical nanometrology [26] of periodic granular thin films of thicknesses down to few nanometers [27,28]. Photoacoustics investigations of the *bulk* properties of *nonperiodic* nanogranular films have also been performed in several contexts over granularities ranging from a few nm [4,29,30] to hundreds of nm [31,32] up to the micron scale [33]. As for *interface properties*, photoacoustic investigations mainly focused on *homogeneous* thin films [34–44], nanogranular thin film interfaces remaining relatively unexplored. The difficulty is to address “patched” interfaces as the one emerging between an aperiodic granular film and the adhering substrate, disorder being the critical aspect [29]. Acoustic attenuation times for such an interface are hard to

conceive in analytical terms, calling for full 3D finite element method (FEM) simulations and casting the acoustic wave problem at the interface in scattering terms. These approaches, whenever applicable, do not shed much light on the underlying physics and are hardly implementable to fit photoacoustic data due to computational costs. Furthermore, implementation of full 3D models requires knowledge of the detailed film morphology at the interface which, for the case of aperiodic granular materials, is unknown or very difficult to achieve [30]. Therefore, easy-to-adopt mechanical models are necessary to interpret photoacoustics data, retrieving the interface physical properties and ultimately unveiling the relevant physics ruling the acoustic to structure relation in materials with disordered interfaces. From a general viewpoint, the situation addressed here is complementary to that of acoustic damping from a single nano-object to its supporting substrate [45,46]. For the latter, the experimental is challenging, whereas the modeling is rather straightforward since it relies on a thorough system's knowledge [47,48]. On the contrary, in the present case the experimental is relatively simple [29], the modeling though is the delicate and yet unsolved issue. This is ascribable to the disordered, hence intrinsically undetermined, interface.

A 1D mechanical model for nanogranular thin films adhered to a flat substrate is proposed. The model, addressed as pillar model, is based on a structural interface [49], meaning that a true structure is introduced to mimic the transition region between the NP's film bulk and the underlying substrate. Extrinsic attenuation, i.e., acoustic radiation to the substrate, is assumed to prevail over intrinsic attenuation which is not accounted for. The analytical dispersion relation for the frequencies and lifetimes of the ultrathin film's acoustic

*giulio.benetti@aovr.veneto.it

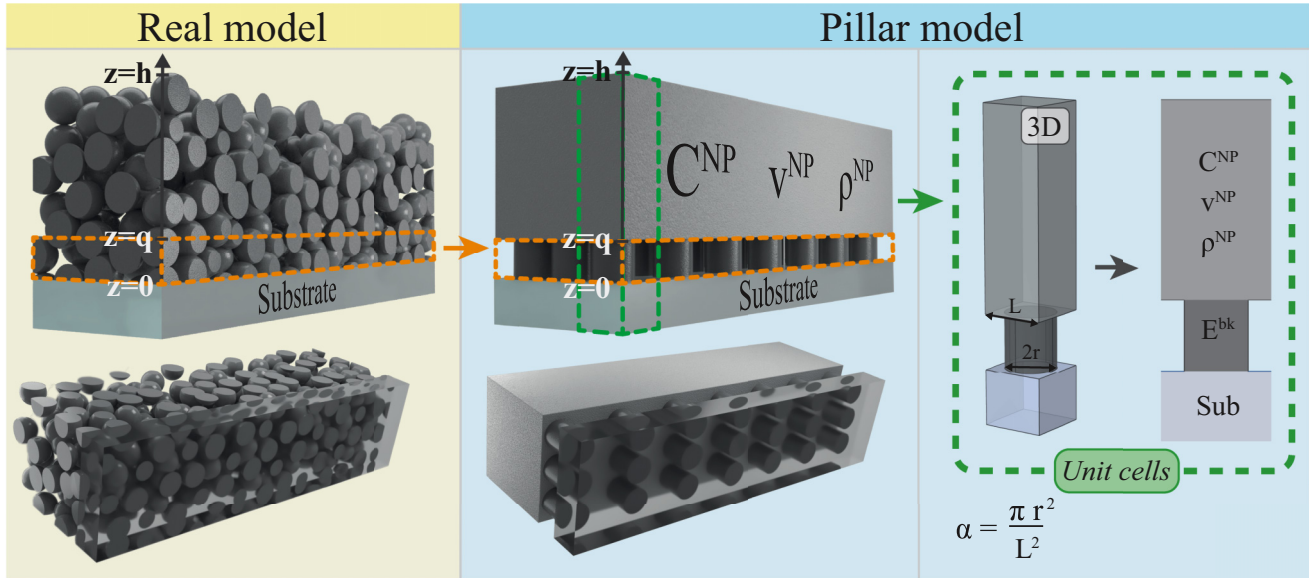


FIG. 1. Left: 3D nanoparticles thin film of thickness h adhered to a semi-infinite substrate. The bottom view, as seen looking across the substrate, highlights the “patched” interface. Center: 3D pillar model: *effective* NP layer ($q < z < h$); pillars layer ($0 < z < q$); semi-infinite substrate ($z < 0$). The NP layer effective density and stiffness tensor are ρ^{NP} and C^{NP} , respectively. The pillars layer density ρ^{bk} and Young modulus E^{bk} are the same as the ones of the material of which the NPs are made (see text). The bottom view, as seen looking across the substrate, highlights the similarity with the patched interface of the real case. Right: Reduction of the periodic 3D pillar model to a single 3D unit cell of base size $L \times L$. The pillar layer filling fraction α is defined as the ratio of the pillar cross-sectional area to that of the unit cell, irrespective of the geometry of the pillar cross section. The image is for illustrative purposes.

breathing modes, i.e., the ones commonly excited in photoacoustic experiments, is obtained in terms of the interface layer physical parameters: interface porosity and layer thickness. The model is successfully benchmarked both against a full 3D FEM model and against experimental photoacoustic data available from the literature on a paradigmatic model system, in which knowledge of mechanical properties at the interface is a key asset in a variety of applications [4,50,51]. A simpler 1D model, addressed as an effective medium approximation model (EMA) and based on an homogenized interface layer, is also provided together with its dispersion relation. Its limits of validity, restrained to small porosities, are discussed at the light of the pillar model. Assuming the granular film made of nanoparticles (NP), the present theoretical scheme is tested for the case of NP radii smaller than the film thicknesses and inferior to the excited breathing modes wavelength.

The pillar model rationalizes the acoustic to structure relation in materials affected by disordered interfaces. The physics is shown to be ruled by the integral of the stresses exchanged across the interfaces rather than their detailed distribution. The pillar model, on one side, furnishes to the experimentalist an experimentally benchmarked, easy-to-adopt analytical tool to extract the interface layer physical parameters upon fitting of the acoustic data. On the other side, upon previous knowledge of the interfacial layer parameters, the model allows retrieving the breathing modes frequencies and lifetimes of a nanogranular coating adhering to a substrate. All these aspects bear both a fundamental and applicative interest across a wide range of fields ranging from condensed matter, material science, to device physics.

II. THE PILLAR MODEL

The mechanical response of a nanoparticle film resting on an infinitely extended substrate (Fig. 1) is analyzed here assuming negligible intrinsic acoustic losses. For the sake of the following discussion three layers are defined: the NP film layer ($q < z < h$), the interfacial layer ($0 < z < q$), and the semi-infinite substrate layer ($z < 0$). The problem is considered one dimensional, as is the case for photoacoustic measurements on ultrathin films [29,41,52]. The only nonzero component of the displacement field $u_z^\#(z, t)$ satisfies the classic wave equation:

$$\frac{\partial^2 u_z^\#(z, t)}{\partial t^2} = v_z^{\#2} \frac{\partial^2 u_z^\#(z, t)}{\partial z^2}, \quad (1)$$

where $u_z^\#(z, t)$ is the displacement component in the z direction, the hash refers to each layer, and $v_z^\#$ is the velocity of the P wave traveling in such materials. The solution of Eq. (1) can be written as

$$u_z^\#(z, t) = U^\#(z)T^\#(t), \quad (2)$$

with

$$\begin{aligned} U^\#(z) &= u_k^\# e^{ik^\#z} + u_{-k}^\# e^{-ik^\#z}, \\ T^\#(t) &= u_\omega^\# e^{-i\omega t}, \end{aligned} \quad (3)$$

where i , ω , and $k^\#$ are the imaginary unit, the frequency, and the wave vector, respectively. Substituting Eqs. (2) and (3) into Eq. (1) yields the dispersion relation $\omega^2 = v_z^{\#2} k^{\#2}$. The first and the second terms of $U^\#(z)$ are the regressive and the progressive components of the wave, respectively. The regressive component of the wave in the

substrate is neglected since this layer is considered as infinitely extended in the z direction, a fact accounting for the radiative attenuation of the film's breathing mode towards the substrate.

When dealing with granular solids, like the aforementioned nanoparticle film (Fig. 1, left), imposing a "perfect adhesion" condition (pa) at the film-substrate interface results in a faulty evaluation of their mechanical behavior. Perfect adhesion implies perfect geometrical matching and continuity of stress and displacement. This fault is particularly relevant when addressing the oscillation's damping time, not as much for the oscillation frequency [29]. This can be traced back to the fact that granularity makes the perfect contact condition unlikely to be achieved, whereas a "patched interface" would be more appropriate.

To overcome this issue, the pillar model is introduced (Fig. 1, center). The pillar model partitions the nanogranular film of thickness h (Fig. 1, left) into three layers (Fig. 1, center). The actual NP film layer $q < z < h$ is accounted for introducing an *effective* homogeneous and isotropic thin film layer extending in the same range. The real NP film morphology is granular rather than homogeneous, nevertheless simulating the real NP film with an homogeneous one allows defining an effective density ρ^{NP} and an effective stiffness tensor C^{NP} . These constants may be retrieved either from experiments [29] or theory [4,30]. The key element in the model is the introduction of a layer of pillars (dashed orange layer in Fig. 1, center), extending in the range $0 < z < q$ and intended to mimic the mechanics in the interfacial layer, i.e., at the interface between the actual film and the substrate (dashed orange layer in Fig. 1, left). The pillars density ρ^{bk} and Young modulus E^{bk} are taken as the ones of the real material of which the NPs are made of. The pillar mechanical properties hence differ from that of the effective NP thin film layer. The pillar layer adheres to a semi-infinite substrate $z < 0$.

The velocity v_z^{NP} of a P wave in the NP film layer is proportional to the coefficient C_{11}^{NP} since transversal contraction is prevented:

$$v_z^{\text{NP}} = \sqrt{\frac{C_{11}^{\text{NP}}}{\rho^{\text{NP}}}}, \quad (4)$$

while the velocity of a P wave in the pillars is proportional to the Young modulus E^{bk} since they are free to expand transversely:

$$v_z^{\text{NP}} = \sqrt{\frac{E^{bk}}{\rho^{bk}}}. \quad (5)$$

For the pillar model, the boundary conditions are the following:

(1) Free standing at the top of the effective NP layer ($z = h$):

$$C_{11}^{\text{NP}} \frac{\partial u_z^{\text{NP}}(h, t)}{\partial z} = 0. \quad (6)$$

(2) Equilibrium at the interface between the effective NP layer and the pillars layer ($z = q$):

$$F^{\text{NP}}(q, t) = F^{\text{pil}}(q, t). \quad (7)$$

(3) Continuity of the displacement at the interface between the effective NP layer and the pillars layer:

$$u_z^{\text{NP}}(q, t) = u_z^{\text{pil}}(q, t). \quad (8)$$

(4) Force equilibrium at the interface between the pillars layer and the sapphire substrate ($z = 0$):

$$F^{\text{pil}}(0, t) = F^{\text{sub}}(0, t). \quad (9)$$

(5) Continuity of the displacement at the interface between the pillars layer and the sapphire substrate:

$$u_z^{\text{pil}}(0, t) = u_z^{\text{sub}}(0, t). \quad (10)$$

It is pinpointed that the continuity of the stresses at the interfaces between the pillars and the two continuous layers is replaced with the balance of their resultant forces F as can be seen appreciated in Eqs. (7) and (9). This is a key point of the model.

Equations (7) and (9) reduce to

$$C_{11}^{\text{NP}} \frac{\partial u_z^{\text{NP}}(q, t)}{\partial z} = \alpha E^{bk} \frac{\partial u_z^{\text{pil}}(q, t)}{\partial z}, \quad (11)$$

$$\alpha E^{bk} \frac{\partial u_z^{\text{pil}}(0, t)}{\partial z} = C_{11}^{\text{sub}} \frac{\partial u_z^{\text{sub}}(0, t)}{\partial z},$$

respectively, where α is the contact ratio between the areas of the two homogeneous layers (substrate and effective NP film) and that of the pillars (see Fig. 1, right), C_{11}^{sub} and C_{11}^{NP} the substrate's and the effective NPs film relevant stiffness tensor's component, respectively. The model is therefore reduced to 1D. It is noteworthy that, despite the fact that the pillars in Fig. 1 are represented with a circular cross section, the definition of the parameter α and the structure of the model do not change if the shape of such cross section is chosen to be different, for instance square shaped rather than circular. Furthermore, the analytical model does not depend on the position of the pillar with respect to the unit cell, despite the fact that the pillars in Fig. 1 are shown at its center. These two aspects are crucial for a model intended to correctly rationalize a disordered interface, where the number of possible NPs dispositions at the interface, i.e., number of microstates or configuration in statistical mechanics terms, is infinite. In photoacoustic experiments for instance, where both the excitation and probing laser beams are much wider than the NP's dimensions, a huge number of possible unit cell's configurations are probed all together within a single measurement. The acoustic problem is therefore not affected by the specific global interface configuration, hence for the pillar model to correctly capture the physics it must not depend on the specific pillar cross-sectional geometry or position within the unit cell.

Enforcing the boundary conditions Eqs. (6)–(10) in Eq. (2) yields the following equation in the complex-valued unknown $\omega(q, \alpha)$:

$$Z^{\text{NP}} - \frac{\alpha E^{bk} \cot\left(\frac{(h-q)\omega}{v_z^{\text{NP}}}\right) \left[v_z^{\text{pil}} Z^{\text{sub}} \cos\left(\frac{q\omega}{v_z^{\text{pil}}}\right) - i \alpha E^{bk} \sin\left(\frac{q\omega}{v_z^{\text{pil}}}\right) \right]}{v_z^{\text{pil}} \left[v_z^{\text{pil}} Z^{\text{sub}} \sin\left(\frac{q\omega}{v_z^{\text{pil}}}\right) + i \alpha E^{bk} \cos\left(\frac{q\omega}{v_z^{\text{pil}}}\right) \right]} = 0, \quad (12)$$

where Z^{NP} and Z^{sub} are the acoustic impedances of the effective NP layer and the substrate, respectively. Actually, Eq. (12) may be solved numerically and yields, for each fixed set of parameters (q, α) , infinitely many solutions $\omega = \omega_n(q, \alpha)$ with $n = \{0, 1, 2, \dots\}$ the index numbering the mode.

Once the total thickness h of the actual real film is assigned, the only free parameters in Eq. (12) are the height of the pillars q and the contact ratio between the two homogeneous layers and the pillars α . The relations linking the period of vibration $T_n(q, \alpha)$ and the wave decay time $\tau_n(q, \alpha)$ to the n -mode complex-valued angular frequency are

$$T_n(q, \alpha) = \frac{2\pi}{\text{Re}[\omega_n(q, \alpha)]},$$

$$\tau_n(q, \alpha) = \frac{1}{\text{Im}[\omega_n(q, \alpha)]}. \quad (13)$$

The intuitive idea underlying the pillar model stands for the possibility to reduce the full 3D acoustic scattering problem, involving a disordered interface, to a more amenable 1D one. This approximation is meaningful provided the detailed distribution of stresses across the interface does not affect the solution in terms of quasimode period and lifetime. As a matter of fact, the 1D model retains information on the integral of the stresses exchanged across the interfaces rather than their detailed distribution. This key point finds its microscopic justification on the fact that the acoustic problem is not affected by the specific interface configuration, as earlier addressed.

The pillar model is more evolved with respect to spring-based interface models, which are commonly exploited to mimic imperfect interfaces, see for instance the seminal work of Ref. [53]. In the present case, the pillar has rigidity $\alpha E^{bk} L^2/q$, which, contrary to the spring rigidity, arises from the specific interface geometrical and physical characteristics. Furthermore, the pillars correctly account for inertia, the mass being distributed as opposed to concentrated, as is the case for mass-spring interface models and alike.

TABLE I. Summary of the mechanical properties of the layers.

ρ^{NP}	8400 kg m ⁻³
v_z^{NP}	2880 m s ⁻¹
Z^{NP}	2.42×10^7 kg s ⁻¹ m ⁻²
C_{11}^{NP}	6.96×10^{10} Pa
ρ^{bk}	10 490 kg m ⁻³
v_z^{bk}	2740 m s ⁻¹
Z^{bk}	2.87×10^7 kg s ⁻¹ m ⁻²
E^{bk}	7.88×10^{10} Pa
ρ^{sub}	3986 kg m ⁻³
v_z^{sub}	11260 m s ⁻¹
Z^{sub}	4.49×10^7 kg s ⁻¹ m ⁻²

A. The pillar model: Case study

The pillar model is exemplified here for the case of a real granular thin film [29] made of pure Ag NPs ~ 6 nm in diameter, total film thickness $h = 50$ nm, filling factor 0.8, and adhered to a sapphire substrate, (0001) α -Al₂O₃ single crystal, of acoustic impedance Z^{sub} . Acoustic damping was shown to be due to extrinsic losses, a condition that must be met in order for Eq. (12) to be applicable. The NP film is well mimicked by an homogeneous effective film of known mechanical properties: v_z^{NP} , ρ^{NP} , and Z^{NP} . The concept of NP film is meaningful beyond the first two deposited layers of NPs, leading to an interface layer of ~ 12 nm, as detailed in Ref. [30]. A value of $q = 12$ nm is therefore assumed for the pillars, which are made of pure Ag of density ρ^{bk} , Young modulus E^{bk} , and sustain P waves of sound velocity v_z^{bk} . The pillar layer filling factor α is left here as the sole free parameter, Eq. (12) thus linking the complex-valued unknown ω to α . The values of the relevant mechanical properties for this system are reported in Table I.

The oscillation period T_n and lifetime τ_n for the first two modes of the pillar model, $n = \{0, 1\}$, are reported versus α as full lines in Figs. 2(a) and 2(b), respectively. For $\alpha = 0.8$ the density of the pillars layer matches the density of the NP layer, the latter being 0.8 that of bulk Ag. Densification of the interface layer with respect to the NP film's bulk was ruled out for the present scenario [30], the maximum value of α is hence here constrained to 0.8. A comment is due here. For the case of cylindrical pillars, a value of $\alpha > \pi/4 \approx 0.78$ implies compenetration of neighboring pillars. This fact does not constitute a problem though, since, as previously discussed, the model is independent on the pillar's cross-section geometry. For instance, for a pillar of square cross section, compenetration is prevented for any value of $\alpha < 1$. For the pillar model, the period and lifetime of a given mode $n = \{0, 1, 2, \dots\}$ (with $n = 0$ meaning $n \rightarrow 0$) are correctly bounded between those of a "free-standing" (*fs*) NP film of thickness $h - q$:

$$T_{n,fs}(\alpha) = \frac{2(h-q)}{v_z^{\text{NP}}} \frac{1}{n}, \quad n = \{0, 1, 2, \dots\}, \quad (14)$$

$$\tau_{n,fs}(\alpha) = \infty, \quad \forall n,$$

and those of the perfect adhesion (*pa*) model:

$$T_{n,pa}(\alpha) = \frac{4h}{v_z^{\text{NP}}} \frac{1}{(1+2n)},$$

$$\tau_{n,pa}(\alpha) = \frac{2h}{v_z^{\text{NP}}} \left| \ln \left(\frac{Z^{\text{sub}} - Z^{\text{NP}}}{Z^{\text{sub}} + Z^{\text{NP}}} \right) \right|^{-1}. \quad (15)$$

Attention is drawn to the fact that actually $\tau_{n,pa}(\alpha)$ is mode independent. Indeed, as α approaches zero so does the pillars cross-sectional area and the pillar model converges to that of a free standing NP film of thickness $h - q$. On the contrary, as α approaches one, and assuming a square cross section for the pillars, the situation converges to that of a perfectly adhering

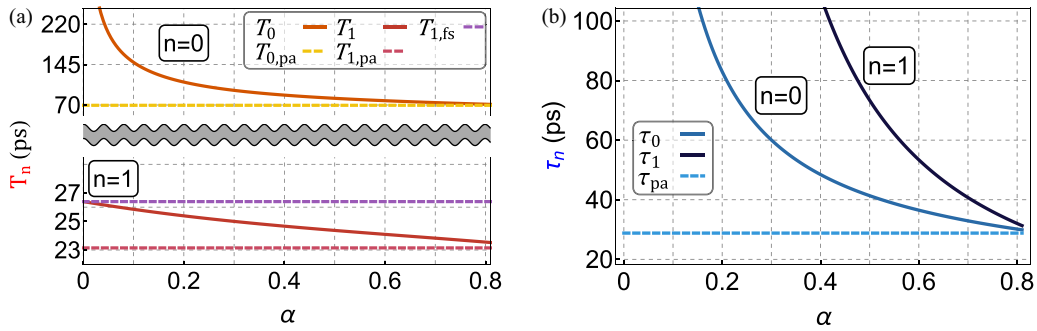


FIG. 2. (a) Period T_n and (b) decay time τ_n versus α for the Ag nanogranular film (see text) with $q = 12$ nm and $h = 50$ nm. The first two modes $n = \{0, 1\}$ are addressed. Pillar model (full lines) and limit cases (dashed lines) obtained for the free-standing (subscript *fs*) and perfect adhesion (subscript *pa*) scenarios, respectively. The y axis in the graph (a) is broken for sake of graphical clarity. The scales above and below the brake are different for ease of representation. The *fs* scenario yields, for mode $n = 0$, an infinite period (corresponding to a film translation), hence it is not reported in (a). The *fs* scenario yields an infinite decay time, hence it is not reported in (b).

film (continuity of displacement and normal stress component at the interface) of thickness h . Specifically, for $n = 0$, T_0 diverges (meaning a film rigid shift) as α approaches zero, as expected for the *fs* film, and is 70 ps for $\alpha = 0.8$, which is converging to the period of the fundamental mode $T_{0,pa}$ for the *pa* case, see Fig. 2(a). On the same footing, the mode lifetime τ_0 diverges upon approaching the *fs* limit, whereas it approaches the lifetime of the *pa* film $\tau_{pa} \sim 30$ ps for $\alpha = 0.8$, regardless of the specific mode, see Fig. 2(b). For $n = 1$, T_1 evolves from $T_{1,fs} = 27$ ps, for $\alpha = 0$, to close to $T_{1,pa} = 23$ ps, for $\alpha = 0.8$. The small gap between T_1 and $T_{1,pa}$ is due to the fact that wave propagation is governed by E^{bk} in the pillars layer and by C_{11}^{NP} in the NP film, see Fig. 2(a). As for the lifetime, τ_1 qualitatively behaves as τ_0 with respect to the *fs* and *pa* cases. Interestingly, $\tau_1 > \tau_0$ over the entire range of α values, see Fig. 2(b).

The present discussion clearly demonstrates that the mode lifetime, rather than its oscillation period, is mostly sensitive to the interface morphology. For instance, with reference to $n = 1$, varying α so as to evolve from the *fs* to the *pa* film, the relative variation in the oscillation period is $\Delta T_1/T_1 \sim 17\%$, whereas the relative variation in lifetime $\Delta \tau_1/\tau_1$ is infinite. This also explains why, in previous photoacoustics experiments performed on granular thin films, the *pa* model was able to correctly address, within the error bar, the breathing mode oscillation period but failed in reproducing the lifetime [29]. Furthermore, it shows that the pillar model behaves correctly reproducing the *fs* and *pa* cases.

B. The pillar model: Parametric study

Typically, when undertaking an acoustic or photoacoustic investigation of the mechanical properties of ultrathin films, one measures the breathing mode period and lifetime of a specific mode n over varying film's thicknesses h . The interface layer morphology, accounted for by the interface layer filling factor α and its thickness q , may therefore be retrieved from fitting of the experimental data exploiting the pillar model. It is therefore important to undertake a parametric study to inspect how the parameters α and q affect $T_n(h)$ and $\tau_n(h)$. The calculations are performed here assuming the mechanical properties of the granular NP film addressed

above. For sake of exemplification, we focus here on mode $n = 1$, which was the best characterized mode in previous experimental work. $T_1(h; q, \alpha)$ and $\tau_1(h; q, \alpha)$ are reported versus the total thickness h of the NP layer for a fixed value of $\alpha = 0.68$ (the value that gives optimal fitting of the photoacoustic data) while varying the parameter q across the set of values $\{6, 8, 10, 12\}$ nm [Fig. 3(a)] and, vice versa, fixing a value of $q = 12$ nm (the value that gives optimal fitting of the photoacoustic data) while varying α across the set of values $\{0.60, 0.65, 0.70, 0.75\}$ [Fig. 3(b)]. $T_1(h; q, \alpha)$ and $\tau_1(h; q, \alpha)$ are also reported for lower values of α and a fixed q in the Supplemental Material [54]. This set of values has been chosen around the best fitting value $\alpha = 0.68$, arising from fitting the experimental data pertaining to the sample addressed here, as detailed further on. Within these parameters ranges and with reference to $\tau_1(h; q, \alpha)$, the two parameters act rather independently, q and α governing the position of the inflection point [see Fig. 3(a)] and the tangent at the very same point [see Fig. 3(b)], respectively. Indeed, for a fixed α , the flex moves towards higher h values as q increases, whereas, for a fixed q , as α approaches unity, the tangent's slope decreases, attaining an asymptotic value concomitantly with the curvature reaching zero. Far enough from the inflection point, $\tau_1(h; \alpha)$ is rather linear with h [see Fig. 3(b)]. As for the periods $T_1(h; q, \alpha)$, the differences are not appreciable throughout the presently explored range, see Fig. 3 dashed orange blend lines.

Solutions obtained over a wider α and h span are reported in Fig. 4 for the same value of $q = 12$ nm. Two features clearly arise. First, when extending the analysis to include also smaller α , i.e., slender pillars, a resonance in $\tau_1(h; q, \alpha)$ clearly emerges, and grows more pronounced as the pillar gets slender, see the decay times curve for α values of 0.4, 0.25, 0.2. This fact may be intuitively rationalized considering that, as the pillar gets slender, the situation approaches that of a free-standing film. Formally, the pillar stiffness decreases proportionally to its cross section (that scales with α), resulting in a monotonic reduction of the mechanical wave propagation speed, ultimately extending the quasimode lifetime.

These resonances stand out also in the mode's Q factor, a feature recently observed also in the context of a single nanodisk adhered to a substrate [55]. Second, for large enough

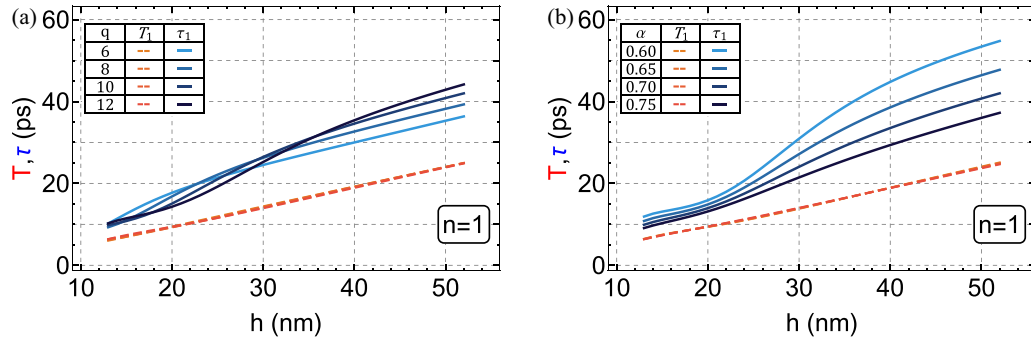


FIG. 3. $T_1(h; q, \alpha)$ and $\tau_1(h; q, \alpha)$ versus h for $n = 1$ for the Ag nanogranular film: (a) Fixed $\alpha = 0.68$ while varying q (expressed in nm). (b) Fixed $q = 12$ nm for a limited span of α values centered around the best fitting value $\alpha = 0.68$. The plots of $T_1(h; q, \alpha)$ (dashed line, orange color range) graphically overlap, not so for $\tau_1(h; q, \alpha)$ (continuous line, blue color range).

values of h , that is once the pillar length becomes negligible with respect the total thickness of the nanoparticle film, $\tau_1(h; q, \alpha)$ scales rather linearly with h . In this h range also the minute differences in the periods $T_1(h; q, \alpha)$ for different α values can be appreciated, see Fig. 4 orange blend curves.

C. Pillar model benchmarking: Fitting photoacoustic data

The pillar model is now deployed to fit photoacoustic data acquired on nanogranular films of different thicknesses [29]. The samples are the same as the one addressed in the case study. These samples constitute an ideal system for benchmarking purposes. The peculiarities of the deposition method [56] allow us to obtain solvent-free and ultrapure nanoporous films, avoiding the synthesis-related complications involved in other methods. Furthermore, these films have been fully characterized in terms of compositional, structural, morphological, and mechanical properties. On a general basis, the interface layer properties are the ones which prove harder to access. Whereas the NP film layer filling factor may be retrieved employing a variety of techniques, such as x-ray reflectivity [29], environmental ellipsometric porosimetry [57], and combining the Brunauer-Emmett-Teller method (BET) with atomic force microscopy (AFM) [58], the interface layer filling factor α and thickness q escape direct inspection. Only recently were the latter quantities operatively defined and estimated via a combined transmission electromicroscopy (TEM)

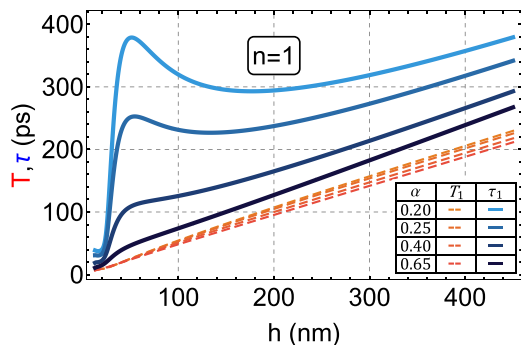


FIG. 4. $T_1(h; q, \alpha)$ and $\tau_1(h; q, \alpha)$ versus an extended h range for $n = 1$ for the Ag nanogranular film: $q = 12$ nm and α values over an extended span.

and molecular dynamic (MD) investigation performed on the samples addressed here [30]. Specifically, the interface layer thickness is defined as the minimal film thickness beyond which the slice filling factors, calculated for thicker films, overlap, as addressed in all details in [30].

The pillar model is benchmarked by letting q and α be fitting parameters and maximizing the likelihood between the h -dependent functions $T_1(h; q, \alpha)$ and $\tau_1(h; q, \alpha)$ and the experimental values $T_{1,\text{expt}}(h)$ and $\tau_{1,\text{expt}}(h)$, reported in [29]. Results are reported in Fig. 5 for the best fit values of $q = 12$ nm and $\alpha = 0.68$ (continuous lines) together with the experimental data (markers). Fitting eight data points with two free parameters may not be ideal, nevertheless, the best fit parameters are fully consistent with the values that have been retrieved by other means: $q = 12$ nm and $\alpha \sim 0.7$ for the interface layer [30]. This is to say that, in the fitting procedure, one could have taken α as the sole fitting parameter, or even fixed all the parameters from previous knowledge, still landing on the experimental data with the theoretical curves calculated adopting the pillar model. The value $\tau_1(h = 15 \text{ nm})$ falls at the edge of the error bar of $\tau_{1,\text{expt}}(h = 15 \text{ nm})$: for $h = 15$ nm the effective NP layer is only 3 nm thick, approaching the limit where only an interface layer exists and the concept of a film

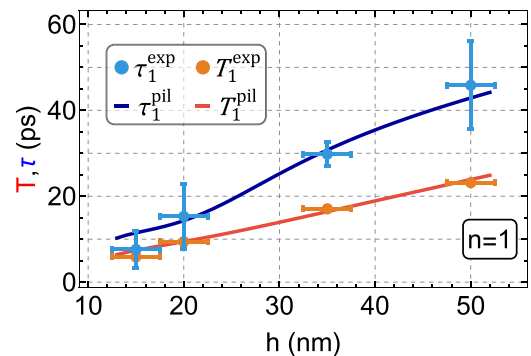


FIG. 5. Pillar model's best fit solution for mode $n = 1$ for the Ag nanogranular film: $T_1(h; q, \alpha)$ (continuous orange line) and $\tau_1(h; q, \alpha)$ (continuous blue line) vs h plotted for the best fit parameters $q = 12$ nm and $\alpha = 0.68$. The fitting is performed against the experimental data from [29]: $T_{1,\text{expt}}(h)$ (light orange dots) and $\tau_{1,\text{expt}}(h)$ (light blue dots). The error bars on the measured oscillation periods, although present, are too small to be appreciated.

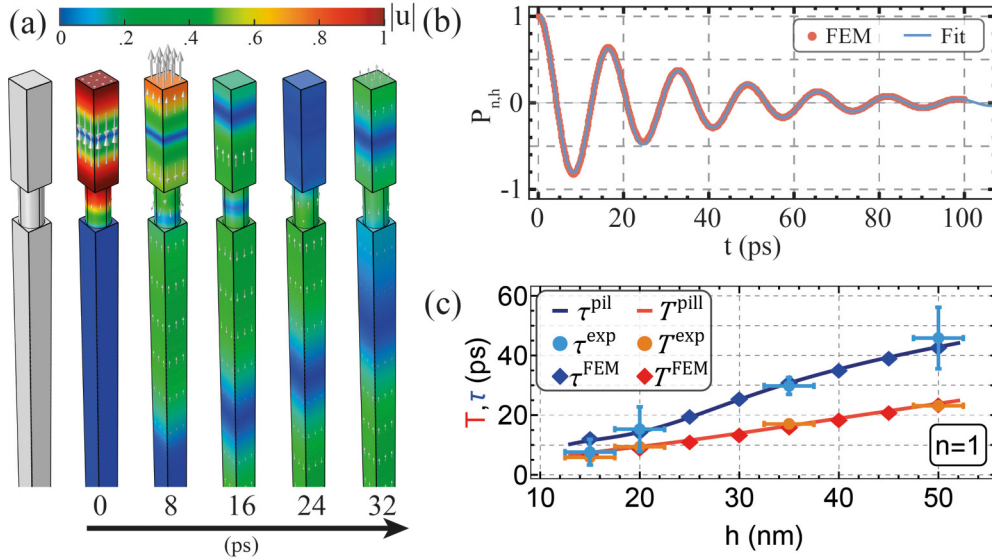


FIG. 6. Ag nanogranular film (see text). (a) Simulation domain and displacement field $\mathbf{u}_{n,h}(\mathbf{r}, t)$ (arrows) and modulus (colormap) at increasing times for $n = 1$, $h = 40$ nm, and $q = 12$ nm. The displacement $\mathbf{u}_{1,40}(\mathbf{r}, t = 0)$ is constructed to match, for $z \geq 0$, the film's eigenmode $n = 1$. (b) Normalized projection coefficient $P_{1,40}$ vs time for the case represented in (a) (full red dots); its fit with a damped oscillation of period T and decay time τ (blue line). (c) Periods and decay times vs film thickness: FEM simulations (diamonds), pillar model (solid lines), and experimental data from [29] (dots).

becomes questionable. Summarizing, the pillar model allows rationalizing the experimental data, the best fitting parameter being fully consistent with the values expected from previous knowledge.

D. Pillar model benchmarking: 3D pillar model solved by FEM

We now compare the analytical 1D pillar model, addressed so far as the pillar model for brevity, against FEM simulations performed on the 3D pillar model. The scope is twofold. A first quest is whether the reduction from a full 3D pillar model (see Fig. 1, center), where acoustic wave scattering is accounted for, to the 1D pillar model expressed by Eq. (12), which does not account for scattering, is justified for the case of low n modes. Furthermore, the 3D model accounts for the distribution of stresses across the interfaces, whereas the pillar model retains information on the integral of the stresses only. Comparing results obtained from the pillar model against those of 3D FEM simulations would enable confirming the soundness of these approximations. Second, although the pillar model benchmarked remarkably well against existing experimental data, the quest stands as whether the model remains effective across a wider range of interface layer filling factors, while keeping the NP film layer mechanical properties unaltered, (i.e. fixed NP's film filling fraction), a situation for which we lack experimental data. In this sense comparing against FEM simulations constitute a valid alternative.

We then proceed as follows. As a validation step, we first implement FEM simulations on the 3D pillar model, mimicking the situations for which experimental data are available. That is we excite a specific film breathing mode $n = 1$ and, subsequently, simulate its temporal evolution throughout the sample, now comprising the substrate as well, thus accessing the quasideigenmode oscillation period, lifetime, and quality factor. As a matter of fact, once the substrate is accounted

for, the film breathing mode becomes a quasimode radiating acoustic energy into the substrate. The results will be benchmarked against both, those of the pillar model and the experimental ones. We then run similar simulations varying the pillar layer filling fraction α for a fixed film thickness $h = 50$ nm and compare the results against the values obtained from the pillar model.

To this end we first consider the 3D pillar model (see Fig. 1, right) mimicking the samples on which experiments were performed and for which $q = 12$ nm and $\alpha = 0.68$ were obtained.

Geometry. The 3D unit cell geometry, reported in Fig. 6(a) and in right panel of Fig. 1, is composed of three domains and has base dimensions $L \times L$. Domain sub ($-5 \mu\text{m} < z < 0$) consists of a $5\text{-}\mu\text{m}$ -thick sapphire substrate. This value has been chosen long enough so as to avoid any wave front reflection from the bottom of sapphire within the time span of the simulated dynamics. For the sake of visualization only a small part of it is shown. Domain pil ($0 < z < q$) consists of a pure Ag cylindrical pillar of height q and radius $r_{\text{pil}} = L\sqrt{\alpha/\pi}$. We take $r_{\text{pil}} = 3.2$ nm, consistent with the NPs radius composing the experimentally investigated films, thus resulting in $L = 7$ nm. Domain NP ($q < z < h$) consists of the effective NP layer of thickness $h - q$.

Materials properties. As for the domains mechanical properties, the densities and elastic constants for sapphire and polycrystalline Ag are taken for the substrate and for the pillar, respectively, whereas the effective NP layer is attributed to the density ρ^{NP} and the elastic tensor components $C_{11} = 6.96 \times 10^{10}$ GPa, taken from [29], and $C_{44} = 1,86 \times 10^{10}$ GPa, calculated from Budiansky homogenization formulas [59] for a volumetric filling factor of 0.8. The C_{44} value is not actually of any relevance, since, given the problem's symmetry to be discussed shortly, the solution is independent on the choice

of C_{44} , as we numerically tested. The adopted values for the above-mentioned quantities are reported in Table I.

Boundary conditions. A zero-displacement boundary condition is enforced at the “sub” bottom surface. The “NP” top surface is taken stress free. At the portion of the bottom surface of NP not in contact with the pillar ($z = q^+$ and $\sqrt{x^2 + y^2} > r_{\text{pil}}$), a stress-free boundary condition is enforced together with the constraint that the z component of the displacement (w) must be spatially constant along the x - y plane (rigid connector). Actually the rigid connector condition does not affect the result but slightly improves the computation time. The displacement field component normal to the lateral boundaries of sub and NP is fixed to zero due to the system periodicity and the experimental excitation symmetry. The pillar’s wall is constrained to move in the vertical (i.e., the direction normal to the substrate) and radial direction only, so as to impede pillar torsion. These boundary conditions have been chosen so as to be consistent with the pillar model. Furthermore, the boundary conditions in both models, together with the irrelevance of the choice of C_{44} in the domain NP, are consistent with the displacement and stress fields symmetry triggered by an excitation mechanics such as that of a laser pulse, of waist much greater than the overall film thickness h , impinging at normal incidence on the film.

Film’s quasimode period, lifetime, and Q factor. We first calculate the set of eigenmodes $\{\tilde{\mathbf{u}}_{n,h}(\mathbf{r})\}$ solutions of the acoustic eigenvalue problem for the domain $\text{pil} \cup \text{NP}$ of height h :

$$\nabla \cdot [\mathbf{c}(\mathbf{r}) : \nabla \tilde{\mathbf{u}}_{n,h}(\mathbf{r})] = -\rho(\mathbf{r})\omega_i^2 \tilde{\mathbf{u}}_{n,h}(\mathbf{r}), \quad (16)$$

where the integrals are actually calculated on the film’s volume V_{film} , since the initial displacement in the substrate is null by construction. The introduction of the film density $\rho(\mathbf{r})$ is necessary to obtain a formally correct definition of the scalar product, the eigenvalue problem on the entire domain being of the Sturm-Liouville type.

For instance, for the case of a sample with $h = 40$ nm and focusing on $n = 1$, Fig. 6(a) shows the spatial profile of $\mathbf{u}_{1,40}(\mathbf{r}, t = 0)$ (arrows) and its modulus (colorbar) together with snapshots of its evolution $\mathbf{u}_{1,40}(\mathbf{r}, t)$ taken for increasing times. As time evolves, the film’s quasieigenmode $\mathbf{u}_{1,40}(\mathbf{r}, t = 0)$ fades away, displacement radiating into the substrate. Figure 6(b) reports the corresponding $P_{1,40}(t)$ (full red dots), measuring the overlap between the film’s $n = 1$ mode displacement profile at time $t = 0$ and the actual displacement throughout the sample at any given time t . For the “gedanken” case, in which no acoustic radiation to the substrate occurs, the normalized projection coefficient would oscillate in between 1 and -1 without any damping, $\mathbf{u}_{1,40}(\mathbf{r}, t)$ representing, for $z \geq 0$, the film’s quasieigenmode displacement at different times. The normalized projection coefficient’s maximum would thus be attained for $t = mT$ (the two displacements fields being in phase), it would be zero for $t = (2m + 1)T/4$ (the two displacements fields being in quadrature) and be at its

with $\rho(\mathbf{r})$ and $\mathbf{c}(\mathbf{r})$ the position-dependent mass density and elastic stiffness tensor, respectively, and with zero displacement enforced at the boundary $z = 0$. The latter is a good approximation for an impulsive excitation of the film (for instance upon absorption of an ultrashort laser pulse) when $Z_{\text{sub}} > Z_{\text{pil}}$, as in the present case. The first subscript, n , identifies the film’s eigenmode, the second subscript, h , the film’s thickness expressed in nm.

We then define the initial displacement on the entire simulation domain $\text{sub} \cup \text{pil} \cup \text{NP}$:

$$\mathbf{u}_{n,h}(\mathbf{r}, t = 0) = \begin{cases} A\tilde{\mathbf{u}}_{n,h}(\mathbf{r}), & \forall z \geq 0, \\ 0, & \forall z < 0, \end{cases} \quad (17)$$

where the displacement amplitude A will cancel out in the following analysis. We pinpoint that $\mathbf{u}_{n,h}(\mathbf{r}, t = 0)$ is *not* an eigenmode of the acoustic eigenvalue problem for the domain $\text{sub} \cup \text{pil} \cup \text{NP}$, nevertheless, for $h \geq 0$, it matches the eigenmode of domain $\text{pil} \cup \text{NP}$. The initial velocity field is taken as $\dot{\mathbf{u}}_{n,h}(\mathbf{r}, t = 0) = 0$.

Propagating the initial displacement on the entire unit cell via the Navier equation,

$$\nabla \cdot [\mathbf{c}(\mathbf{r}) : \nabla \mathbf{u}] = \rho(\mathbf{r})\ddot{\mathbf{u}}, \quad (18)$$

we obtain $\mathbf{u}_{n,h}(\mathbf{r}, t)$.

For the sake of retrieving the film’s quasieigenmode decay time we calculate the normalized projection coefficient between modes $\mathbf{u}_{n,h}(\mathbf{r}, t = 0)$ and $\mathbf{u}_{n,h}(\mathbf{r}, t)$:

$$P_{n,h}(t) = \frac{\langle \mathbf{u}_{n,h}(t = 0) | \mathbf{u}_{n,h}(t) \rangle}{\langle \mathbf{u}_{n,h}(t = 0) | \mathbf{u}_{n,h}(t = 0) \rangle} = \frac{\int_V \mathbf{u}_{n,h}(\mathbf{r}, t = 0) \rho(\mathbf{r}) \mathbf{u}_{n,h}(\mathbf{r}, t) d\mathbf{r}}{\int_V \mathbf{u}_{n,h}(\mathbf{r}, t = 0) \rho(\mathbf{r}) \mathbf{u}_{n,h}(\mathbf{r}, t = 0) d\mathbf{r}}, \quad (19)$$

minimum for $t = (2m + 1)T/2$ (the two displacements fields being in antiphase) with $m \in \mathbb{N}_0$. For the real case, in which acoustic radiation is active, the normalized projection coefficient’s oscillation is exponentially damped, its period $T_{1,40}$ and decay time $\tau_{1,40}$ being retrieved fitting the numerical results, see Fig. 6(b), blue line. Running simulations for varying h we thus obtain $T_{n,h}$ and $\tau_{n,h}$, Fig. 6(c) reporting the case for $n = 1$ (filled diamonds). For the sake of comparison, we report on the same graph the data obtained from the analytic solution of the pillar model (full lines) together with the experimental values from ultrafast optoacoustic measurements [29] (filled circles). The three sets of data are in good agreement, pointing to the fact that we correctly addressed the 3D pillar model via FEM and that, at least for $\alpha = 0.68$, the approximations entailed in the pillar model are sound.

Following the same procedure, we now perform FEM simulations on the 3D pillar model varying the pillar layer filling fraction α for a fixed film thickness $h = 50$ nm and for a NP film layer filling factor fixed at 0.68, and compare the results against the values obtained from the pillar model. Figure 7 reports the oscillation period (a), decay time (b), and quality factor (c), $Q_n = \pi(\tau_n/T_n)$, calculated for $n = 0$, where the superscripts FEM and pil stand for FEM simulations and pillar model, respectively. The same quantities,

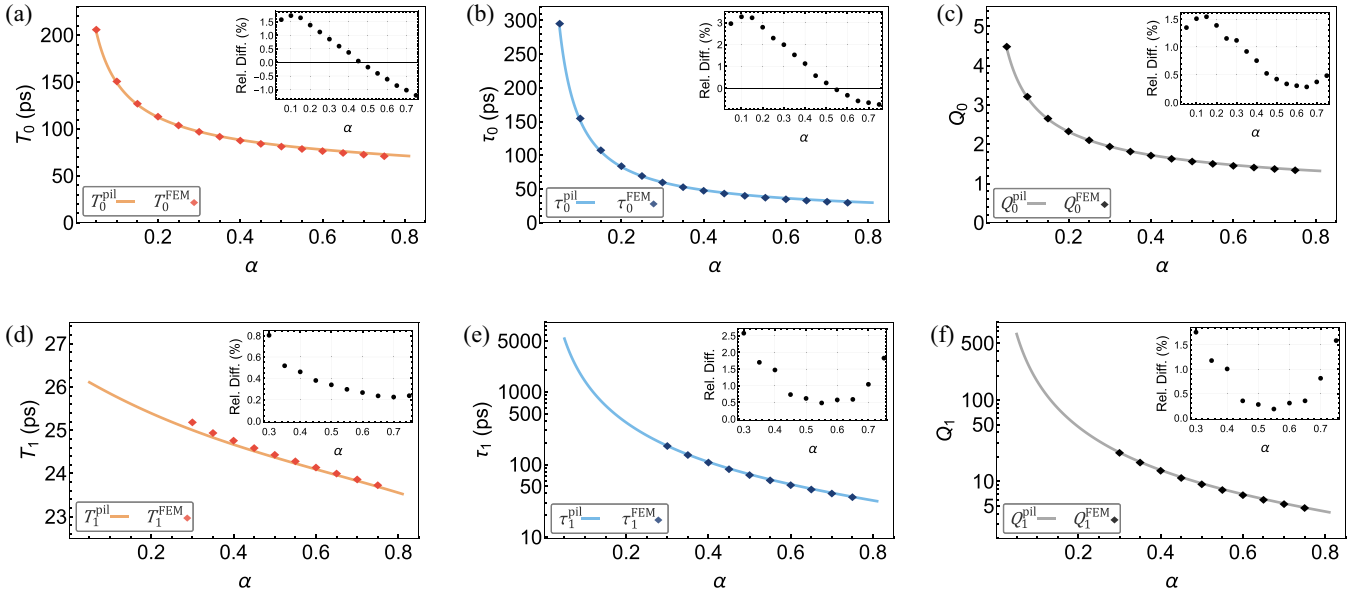


FIG. 7. Ag nanogranular film. Comparison between the oscillation period, decay time, and quality factor obtained from FEM solution of the 3D pillar model (filled diamonds) and the pillar model (full lines) vs the pillar layer filling factor α for a film's thickness $h = 50$ nm. (a) Period, (b) decay time, and (c) quality factor for $n = 0$. (d) Period, (e) decay time (log-lin scale), and (f) quality factor (log-lin scale) for $n = 1$. The insets show the relative difference between the calculated quantities in the two models.

calculated for $n = 1$, are reported throughout Figs. 7(d)–7(f). The two models yield the same results, the relative differences $(X_n^{\text{FEM}} - X_n^{\text{pil}})/X_n^{\text{FEM}}$ with $X = \{T, \tau, Q\}$, amounting, at most, to a few percent, see insets to each graph. For the case $n = 0$ we were able to perform FEM simulations down to $\alpha = 0.05$, whereas for $n = 1$ numerical problems impeded extending simulations below $\alpha = 0.3$. Given the boosting of Q_1 for the latter case, FEM simulations, as the one reported in Fig. 6(b), were performed extending the time range to 500 ps. The overall result is that the analytic 1D pillar model perfectly reproduces the results of the more involved 3D FEM pillar model. Furthermore, the former does not pose any problem for the case of low α values, it is order of magnitudes more efficient in terms of computation times (four orders of magnitudes for the present geometry), and, being analytic, it is much more amenable to fit experimental data and clearly identifies the structural parameters leading the acoustic problem.

For low α values simulations were also performed varying the pillar position within the unit cell xy plane and the pillar cross-sectional geometry (a square instead of a circle while keeping the same surface area), the results remaining unaltered. Those of low α values constitute the worse case scenarios for these tests since a slender pillar can be substantially displaced within the unit cell, whereas only small translations can be tested for the case of plumped pillars, i.e., greater α values. These evidences suggest that results are invariant with respect to the specific disordered interface realization. Specifically, the detailed knowledge of the stresses distribution across the interface does not affect the solution in terms of quasimode period and lifetime, the relevant aspect rather being the integral of the stresses exchanged across the interfaces. The latter supports the physical ansatz implied in the 1D pillar model.

For the sake of completeness, in the Supplemental Material (SM) we also report the modulus of the displacement

$\{|\tilde{\mathbf{u}}_{n,50}(\mathbf{r})|\}$ for the first ($n = 0$) and the second ($n = 1$) film breathing modes for $\alpha = 0.05, 0.4$, and 0.75 [60]. These plots give an idea of the quasibreathing mode evolution from the *quasi-free standing* to the *quasi-perfect adhesion* scenarios.

III. EMA MODEL

In order to display the potential of the pillar model, its broad validity range and its added value with respect to more traditional approaches, a simpler 1D model, addressed as effective medium approximation model (EMA) and based on an homogenized interface layer, is now introduced and its dispersion relation calculated. Its limit of validity, restrained to small porosities, are discussed at the light of the pillar model, showing the need for the latter to correctly access the acoustic to structure relation in granular ultrathin films. The interface layer, previously identified with the pillar layer, is now accounted for via a continuum, isotropic, and homogeneous slab, addressed as effective interface layer, see Fig. 8. The latter mimics an interface granular layer of thickness d , with its solid component made of the same material constituting the NPs and of filling fraction β . The parameters d and β play a similar role as h and α in the pillar model. The elastic properties of the effective interface layer, denoted with an asterisk as a superscript, are calculated on the basis of Budiansky theory [59]. The bulk $K^*(\beta)$ and shear modulus $G^*(\beta)$ are obtained through

$$\sum_{i=1}^n \frac{c_i}{1 + A(\frac{K_i}{K^*} - 1)} = 1, \quad (20)$$

$$\sum_{i=1}^n \frac{c_i}{1 + B(\frac{G_i}{G^*} - 1)} = 1,$$

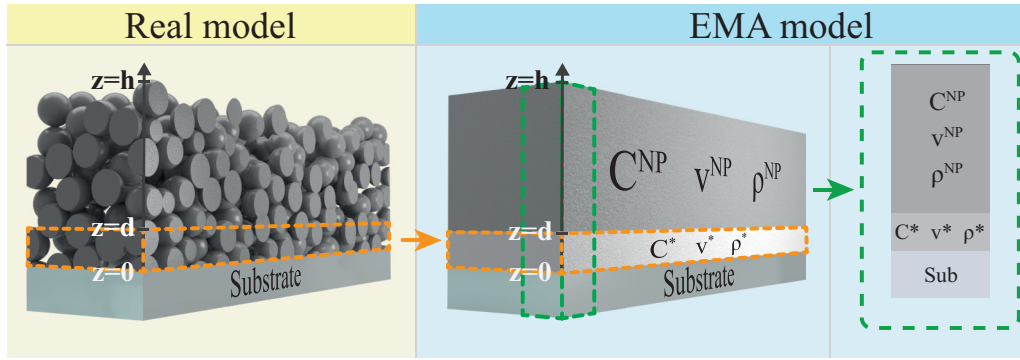


FIG. 8. Left: 3D nanoparticles thin film of thickness d adhered to a semi-infinite substrate. Center: EMA model: effective NP layer ($d < z < h$); effective interface layer ($0 < z < d$); semi-infinite substrate ($z < 0$). The NP layer is the same one addressed in the pillar model. The interface layer has effective mechanical properties C^* , v^* , and ρ^* (see text). The image is for illustrative purposes. Right: 1D sketch of the EMA model.

where the value of A and B are

$$A = \frac{1 + \nu^*(\beta)}{3[1 - \nu^*(\beta)]}, \quad B = \frac{2[4 - 5\nu^*(\beta)]}{15[1 - \nu^*(\beta)]}, \quad (21)$$

in which the Poisson's ratio is expressed via $K^*(\beta)$ and $G^*(\beta)$ by the standard relation

$$\nu^* = \frac{3K^*(\beta) - 2G^*(\beta)}{6K^*(\beta) + 2G^*(\beta)}. \quad (22)$$

In Eq. (20) c_i , K_i , and G_i are the volume fraction, the bulk modulus, and the shear modulus of the phase i , respectively, where, in the present case, $N = 2$, $i = 1$ stands for vacuum and $i = 2$ for the material constituting the NPs (bulk silver in the following), i.e., $c_2 = \beta$. A major pitfall of Budiansky formulas stands on the fact the elastic coefficients vanish when β reaches 0.5, thus setting a limit to the applicability of the EMA model, as will be discussed shortly.

Since the transversal contraction is prevented in the effective interface layer, the P-wave velocity is $v^*(\beta) = \sqrt{\frac{C_{11}^*(\beta)}{\rho^*(\beta)}}$.

The interface boundary conditions for the EMA model are the “perfect adhesion” ones. In the following we summarize the full set of boundary conditions for the EMA model:

- (1) Free standing at the top of the NP layer ($z = h$):

$$C_{11}^{\text{NP}} \frac{\partial u_z^{\text{NP}}(h, t)}{\partial z} = 0. \quad (23)$$

- (2) Continuity of stresses at the interface between the NP layer and the effective homogeneous layer ($z = d$):

$$C_{11}^{\text{NP}} \frac{\partial u_z^{\text{NP}}(d, t)}{\partial z} = C_{11}^*(\beta) \frac{\partial u_z^*(d, t)}{\partial z}. \quad (24)$$

- (3) Continuity of the displacement at the interface between the NP layer and the effective homogeneous layer:

$$u_z^{\text{NP}}(d, t) = u_z^*(d, t). \quad (25)$$

- (4) Continuity of stresses at the interface between the effective homogeneous layer and the sapphire substrate ($z = 0$):

$$C_{11}^*(\beta) \frac{\partial u_z^*(0, t)}{\partial z} = C_{11}^{\text{sub}} \frac{\partial u_z^{\text{sub}}(0, t)}{\partial z}. \quad (26)$$

- (5) Continuity of the displacement condition at the interface between the effective homogeneous layer and the sapphire substrate:

$$u_z^*(0, t) = u_z^{\text{sub}}(0, t). \quad (27)$$

Enforcing the boundary conditions Eqs. (23)–(27) to Eq. (2) yields the following equation in the unknown $\omega(d, \beta)$:

$$Z^{\text{NP}} - \frac{C_{11}^*(\beta) \cot\left(\frac{(h-d)\omega}{v_z^{\text{NP}}(\beta)}\right) \left[v_z^*(\beta) Z^{\text{sub}} \cos\left(\frac{d\omega}{v_z^*(\beta)}\right) - i C_{11}^*(\beta) \sin\left(\frac{d\omega}{v_z^*(\beta)}\right) \right]}{v_z^*(\beta) \left[v_z^*(\beta) Z^{\text{sub}} \sin\left(\frac{d\omega}{v_z^*(\beta)}\right) + i C_{11}^*(\beta) \cos\left(\frac{d\omega}{v_z^*(\beta)}\right) \right]} = 0. \quad (28)$$

Mutatis mutandis from the pillar mode case Eq. (28) may be solved numerically and yields, for each fixed set of parameters (d, β) , infinitely many complex-valued solutions $\omega = \omega_n(d, \beta)$, with $n = \{0, 1, 2, \dots\}$ the index numbering the mode.

Once the total thickness of the NP layer is assigned, the only free parameters in Eq. (28), are the height of the interface layer d and its filling fraction β . The relations linking the pe-

riod of vibration $T_n(d, \beta)$ and the wave decay time $\tau_n(d, \beta)$ to the n -mode complex-valued angular frequency are expressed through Eqs. (13).

Comparison of Eqs. (12) and (28) show that the pillar and EMA models yield the same results provided $d = q$, $\alpha E^{bk} = C_{11}^*(\beta)$, and $v_z^{\text{pil}} = v_z^*(\beta)$. For the case of Ag NPs, the previous equations are satisfied if $\alpha = \beta = 0.770439$.

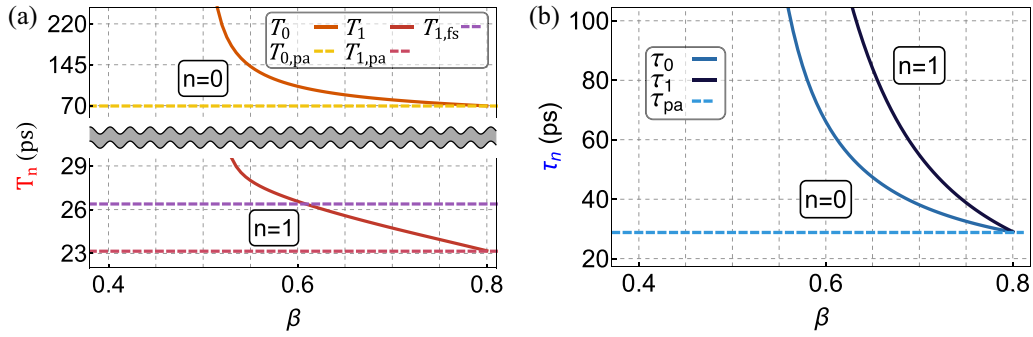


FIG. 9. EMA model. (a) Period T_n and (b) decay time τ_n versus β for the Ag nanogranular film with $d = 12$ nm and $h = 50$ nm. The first two modes $n = 0, 1$ are addressed. EMA model (full lines) and limit cases (dashed lines) obtained for the *fs* and *pa* scenarios, respectively. The y axis in the graph of (a) is broken for the sake of graphical clarity. The scales above and below the brake are different for ease of representation. T_n diverges for $\beta \rightarrow 0.5$, an artifact ascribable to the pitfalls of Budiansky formulas. The *fs* scenario yields, for mode $n = 0$, an infinite period (corresponding to a film translation), hence it is not reported in (a). The *fs* scenario yields an infinite decay time, hence it is not reported in (b).

A. The EMA model: Case study

We now exemplify the EMA model considering the same situation addressed in the case study for the pillar model, the only exception being the replacement of the pillar with the effective homogeneous film of $d = 12$ nm.

The oscillation period T_n and lifetime τ_n for the first two modes of the EMA model $n = \{0, 1\}$ are reported versus β as full lines in Figs. 9(a) and 9(b), respectively. For $\beta = 0.8$ the density of the effective homogeneous layer matches the density of the NP layer, the latter being 0.8 that of bulk Ag. We do not consider interface densification, the maximum β value is thus once again constrained to 0.8. T_n diverges as β approaches 0.5, this being due to the elastic constants becoming null in the Budiansky formula. For the same reason, T_1 is not bound between the values $T_{1,pa}$ and $T_{1,fs}$, as should be the case for a correct model. On the contrary, T_n correctly approaches $T_{1,pa} = 23$ ps for $\beta \rightarrow 0.8$, that is when the interface layer becomes identical to the NPs layer. As for the lifetime, τ_n diverges as β approaches 0.5, again due to the pitfalls of Budiansky formulas.

B. The EMA model: Parametric study

We here repeat the same parametric study, previously performed for the pillar model, for the case of the EMA model.

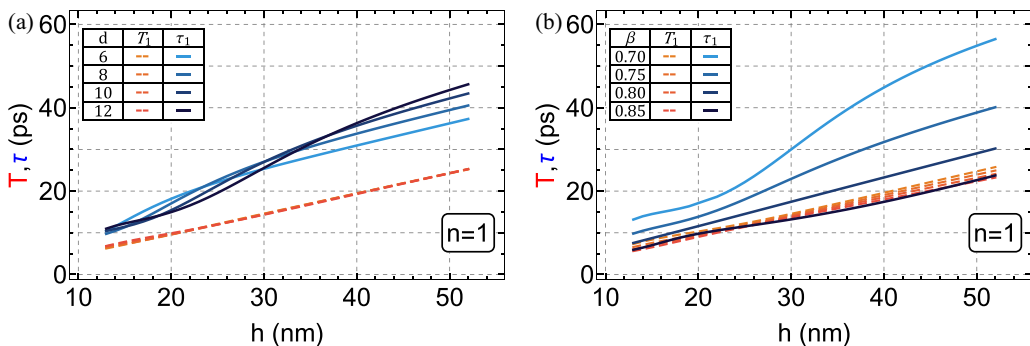


FIG. 10. EMA model. $T_1(h; d, \beta)$ and $\tau_1(h; d, \beta)$ vs h for $n = 1$ for the Ag nanogranular film: (a) Fixed $\beta = 0.73$ while varying d (expressed in nm); and (b) fixed $d = 12$ nm while varying β .

$T_1(h; d, \beta)$ and $\tau_1(h; d, \beta)$ are reported versus the total thickness h of the NP layer for a fixed value of $\beta = 0.73$ (the value that gives optimal fitting of the photoacoustic data, see SM [61]) while varying the parameter d across the set of values $\{6, 8, 10, 12\}$ nm, see Fig. 10(a), and vice versa, fixing a value $d = 12$ nm (the value that gives optimal fitting of the photoacoustic data, see SM [61]) and varying β across the set of values $\{0.70, 0.75, 0.80, 0.85\}$, see Fig. 10(b). Figure 10 shows the same salient features observed for the pillar model in Fig. 3: the position of the inflection point and the magnitude of the tangent in such a point being governed quite independently by d and β , respectively.

C. Pillar vs EMA model

The pillar model is more adherent to physical reality than the EMA model and, contrary to the latter, is reliable across the entire spectrum of interface filling factor values. The EMA model suffers a major drawback in that both the oscillation periods and decay times diverge as the interface layer filling factor approaches 0.5. The EMA and pillar models yields the same results for a very specific value of the layer filling fraction, which happens to be ~ 0.77 for the case investigated here. The EMA model yields reasonable predictions for small departures of β from these values and, in this range, its control parameters work like the ones of the pillar model. For greater

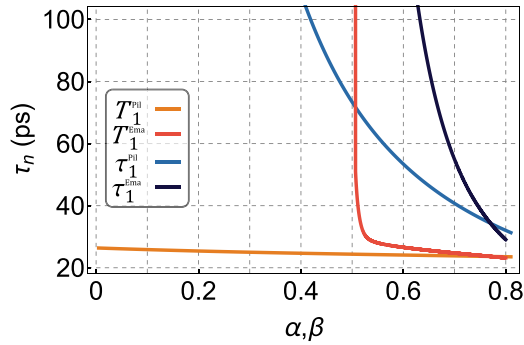


FIG. 11. Ag nanogranular film with $q = 12$ nm (pillar), $d = 12$ nm (EMA) and $h = 50$ nm. Decay time, τ_1^{pil} , and oscillation period, T_1^{pil} , versus α (pillar model); decay time, τ_1^{EMA} , and oscillation period, T_1^{EMA} , versus β (EMA model). The two models coincide for $\alpha = \beta \approx 0.77$.

departures of β from the optimal value, the EMA model fails. Figure 11 summarizes well these points, reporting, on the same graph and for the same sample T_1^{pil} and τ_1^{pil} versus α , for the pillar model, and T_1^{EMA} and τ_1^{EMA} vs β for the EMA model.

IV. CONCLUSIONS AND PERSPECTIVES

The pillar model, a fully analytical 1D acoustic model for nanoporous thin films adhered to a flat substrate, is proposed. The analytical dispersion relation for the frequencies and lifetimes of the film's acoustic breathing modes were obtained in terms of the interface layer's porosity and thickness. The model was successfully benchmarked both against full 3D FEM simulations of a 3D pillar model and photoacoustic data available from the literature on an archetypal model system. The interface mechanical properties of the experimental model system itself bear great applicative relevance, as outlined in recent literature. In order to assess the potential of the pillar model and its broad validity range, its performance was compared against a simpler 1D analytical model, addressed as EMA model, based on an homogenized interface layer of Budiansky type. The limits of applicability of the EMA model were addressed, together with the necessity of deploying the pillar model for most filling factors.

The results reported here are relevant both under a fundamental and applicative stand point. As for the former, the pillar model provides a vivid physical representation of the acoustic of porous thin films and its controlling parameters. More generally, it may be deployed to access the acoustic to structure relation in materials affected by disordered interfaces. The model showed that the physics is primarily dictated by the integral of the stresses exchanged across the interfaces rather than their detailed distribution. Being fully analytical and 1D,

the model is computationally very efficient and particularly amenable to fit experimental quasibreathing mode periods and lifetimes. The model allows accessing the interface layer parameters, which proved challenging to retrieve otherwise. On the other hand, should the porous film morphology been known *a priori*, the model correctly predicts its acoustic response. As for applications, knowledge of granular thin films interfaces adhered to a substrate is of paramount importance in a variety of sectors. Just to mention a few, the NP interface layer rules the adhesion properties of bactericidal coatings [51,62], both the mechanical and the electrical endurance of bendable transparent conductive oxides [50], and conductive NPs films produced by inkjet techniques [63] and the sensitivity of photoacoustics sensors [4].

The pillar model is scale invariant and may thus be deployed to investigate systems of greater dimensions, ranging from porous foams for vibration transmission control, to rock sediments laying on a continuous bed, to seismological scenarios [64]. Furthermore, the model is applicable, beyond the case of granular materials, to any patched interface. This is the case, for instance, when acoustically addressing the wrinkled interface that may arise between a 2D or a few layers material and its supporting substrate [65], when investigating the acoustic properties of thin films suspended on pillars [66], or when inspecting for the presence of PMMA residues between a nanopatterned structure, fabricated via e-beam, lithography, and the substrate it adheres to, an issue of the utmost importance in post-processing quality control.

The pillar model also provides a connection to the adhesion forces. Even though a direct comparison with the pull-off force, as provided by the most common adhesion models (JKR [67], DMT [68]), is not straightforward, a simplified average pull-off pressure estimate is presented in the SM [69].

ACKNOWLEDGMENTS

All the authors are grateful to Prof. Bigoni for enlightening discussions regarding the pillar model. G.R. acknowledge funding from the French Research Agency ANR, METAS-MART (ANR-17CE08-0006), and the support from IDEX-LYON in the framework of the Programme Investissement d'Avenir (ANR-16-IDEX-0005). C.G. and L.G. acknowledge support from Università Cattolica del Sacro Cuore through D.2.2 and D.3.1. C.G. acknowledges financial support from MIUR through the PRIN 2017 program (Prot. 20172H2SC4-005). F.B. acknowledges financial support from Université de Lyon in the frame of the IDEXLYON Project (ANR-16-IDEX-0005) and from Université Claude Bernard Lyon 1 through the BQR Accueil EC 2019 grant. L.G. acknowledges support from Université de Lyon as an Invited Professor. The authors thank Michael Cappozzo for graphical support in realizing 3D renderings of the different models.

- [1] W. J. Stark, P. R. Stoessel, W. Wohlleben, and A. Hafner, Industrial applications of nanoparticles, *Chem. Soc. Rev.* **44**, 5793 (2015).
 [2] G. Benetti, E. Cavaliere, R. Brescia, S. Salassi, R. Ferrando, A. Vantomme, L. Pallecchi, S. Pollini, S. Boncompagni, B. Fortuni *et al.*, Tailored Ag–Cu–Mg multielemental

nanoparticles for wide-spectrum antibacterial coating, *Nanoscale* **11**, 1626 (2019).

- [3] S. M. Villa, V. M. Mazzola, T. Santaniello, E. Locatelli, M. Maturi, L. Migliorini, I. Monaco, C. Lenardi, M. Comes Franchini, and P. Milani, Soft piezoelectric/piezoelectric nanocomposites based on ionogel/BaTiO₃ nanoparticles for low

- frequency and directional discriminative pressure sensing, *ACS Macro Lett.* **8**, 414 (2019).
- [4] G. Benetti, M. Gandolfi, M. J. Van Bael, L. Gavioli, C. Giannetti, C. Caddeo, and F. Banfi, Photoacoustic sensing of trapped fluids in nanoporous thin films: Device engineering and sensing scheme, *ACS Appl. Mater. Interfaces* **10**, 27947 (2018).
- [5] W. Huang, Y. Cao, Y. Chen, J. Peng, X. Lai, and J. Tu, Fast synthesis of porous NiCo₂O₄ hollow nanospheres for a high-sensitivity non-enzymatic glucose sensor, *Appl. Surf. Sci.* **396**, 804 (2017).
- [6] N. Nasiri, R. Bo, T. F. Hung, V. A. Roy, L. Fu, and A. Tricoli, Tunable band-selective uv-photodetectors by 3D self-assembly of heterogeneous nanoparticle networks, *Adv. Funct. Mater.* **26**, 7359 (2016).
- [7] C. Minnai, A. Bellacicca, S. A. Brown, and P. Milani, Facile fabrication of complex networks of memristive devices, *Sci. Rep.* **7**, 1 (2017).
- [8] F. Caruso, A. Bellacicca, and P. Milani, High-throughput shadow mask printing of passive electrical components on paper by supersonic cluster beam deposition, *Appl. Phys. Lett.* **108**, 163501 (2016).
- [9] T. Santaniello and P. Milani, Additive nano-manufacturing of 3D printed electronics using supersonic cluster beam deposition, in *Frontiers of Nanoscience* (Elsevier, Amsterdam, 2020), Vol. 15, pp. 313–333.
- [10] M. Mirigliano, F. Borghi, A. Podestà, A. Antidormi, L. Colombo, and P. Milani, Non-ohmic behavior and resistive switching of Au cluster-assembled films beyond the percolation threshold, *Nanoscale Adv.* **1**, 3119 (2019).
- [11] W. Tarantino and L. Colombo, Modeling resistive switching in nanogranular metal films, *Phys. Rev. Research* **2**, 043389 (2020).
- [12] M. Mirigliano and P. Milani, Electrical conduction in nanogranular cluster-assembled metallic films, *Adv. Phys. X* **6**, 1908847 (2021).
- [13] V. Tournat and V. Gusev, Acoustics of unconsolidated model granular media: An overview of recent results and several open problems, *Acta Acustica united with Acustica* **96**, 208 (2010).
- [14] N. Boechler, Dynamics of microscale granular crystals, in *Micro and Nanomechanics*, Vol. 5 (Springer, Berlin, 2017), pp. 73–77.
- [15] F. Allein, V. Tournat, V. E. Gusev, and G. Theocharis, Tunable magneto-granular phononic crystals, *Appl. Phys. Lett.* **108**, 161903 (2016).
- [16] M. Hiraiwa, M. Abi Ghanem, S. P. Wallen, A. Khanolkar, A. A. Maznev, and N. Boechler, Complex Contact-Based Dynamics of Microsphere Monolayers Revealed by Resonant Attenuation of Surface Acoustic Waves, *Phys. Rev. Lett.* **116**, 198001 (2016).
- [17] A. Vega-Flick, R. A. Duncan, S. P. Wallen, N. Boechler, C. Stelling, M. Retsch, J. J. Alvarado-Gil, K. A. Nelson, and A. A. Maznev, Vibrational dynamics of a two-dimensional microgranular crystal, *Phys. Rev. B* **96**, 024303 (2017).
- [18] S. P. Wallen, A. A. Maznev, and N. Boechler, Dynamics of a monolayer of microspheres on an elastic substrate, *Phys. Rev. B* **92**, 174303 (2015).
- [19] G. Rizzi, M. Collet, F. Demore, B. Eidel, P. Neff, and A. Madeo, Exploring metamaterials' structures through the relaxed micro-morphic model: Switching an acoustic screen into an acoustic absorber, *Frontiers Materials* **7**, 354 (2021).
- [20] B. Graczykowski, N. Vogel, K. Bley, H.-J. Butt, and G. Fytas, Multiband hypersound filtering in two-dimensional colloidal crystals: Adhesion, resonances, and periodicity, *Nano Lett.* **20**, 1883 (2020).
- [21] M. A. Ghanem, A. Khanolkar, H. Zhao, and N. Boechler, Nanocontact tailoring via microlensing enables giant post-fabrication mesoscopic tuning in a self-assembled ultrasonic metamaterial, *Adv. Funct. Mater.* **30**, 1909217 (2020).
- [22] V. Babacic, J. Varghese, E. Coy, E. Kang, M. Pochylski, J. Gapinski, G. Fytas, and B. Graczykowski, Mechanical reinforcement of polymer colloidal crystals by supercritical fluids, *J. Colloid Interface Sci.* **579**, 786 (2020).
- [23] M. Abi Ghanem, A. Khanolkar, S. P. Wallen, M. Helwig, M. Hiraiwa, A. A. Maznev, N. Vogel, and N. Boechler, Longitudinal eigenvibration of multilayer colloidal crystals and the effect of nanoscale contact bridges, *Nanoscale* **11**, 5655 (2019).
- [24] A. Merkel, V. Tournat, and V. Gusev, Dispersion of elastic waves in three-dimensional noncohesive granular phononic crystals: Properties of rotational modes, *Phys. Rev. E* **82**, 031305 (2010).
- [25] M. E. Siemens, Q. Li, M. M. Murnane, H. C. Kapteyn, R. Yang, E. H. Anderson, and K. A. Nelson, High-frequency surface acoustic wave propagation in nanostructures characterized by coherent extreme ultraviolet beams, *Appl. Phys. Lett.* **94**, 093103 (2009).
- [26] D. Nardi, M. Travagliati, M. M. Murnane, H. C. Kapteyn, G. Ferrini, C. Giannetti, and F. Banfi, Impulsively excited surface phononic crystals: A route toward novel sensing schemes, *IEEE Sens. J.* **15**, 5142 (2015).
- [27] B. Abad, J. L. Knobloch, T. D. Frazer, J. N. Hernández-Charpak, H. Y. Cheng, A. J. Grede, N. C. Giebink, T. E. Mallouk, P. Mahale, N. N. Nova *et al.*, Nondestructive measurements of the mechanical and structural properties of nanostructured metalattices, *Nano Lett.* **20**, 3306 (2020).
- [28] T. D. Frazer, J. L. Knobloch, J. N. Hernández-Charpak, K. M. Hoogeboom-Pot, D. Nardi, S. Yazdi, W. Chao, E. H. Anderson, M. K. Tripp, S. W. King *et al.*, Full characterization of ultrathin 5-nm low-k dielectric bilayers: Influence of dopants and surfaces on the mechanical properties, *Phys. Rev. Materials* **4**, 073603 (2020).
- [29] S. Peli, E. Cavaliere, G. Benetti, M. Gandolfi, M. Chiodi, C. Cancellieri, C. Giannetti, G. Ferrini, L. Gavioli, and F. Banfi, Mechanical properties of Ag nanoparticle thin films synthesized by supersonic cluster beam deposition, *J. Phys. Chem. C* **120**, 4673 (2016).
- [30] G. Benetti, C. Caddeo, C. Melis, G. Ferrini, C. Giannetti, N. Winckelmans, S. Bals, M. J. Van Bael, E. Cavaliere, L. Gavioli *et al.*, Bottom-up mechanical nanometrology of granular Ag nanoparticles thin films, *J. Phys. Chem. C* **121**, 22434 (2017).
- [31] A. Ayouch, X. Dieudonné, G. Vaudel, H. Piombini, K. Vallé, V. Gusev, P. Belleville, and P. Ruello, Elasticity of an assembly of disordered nanoparticles interacting via either van der Waals-bonded or covalent-bonded coating layers, *ACS Nano* **6**, 10614 (2012).
- [32] A. Girard, J. Ramade, J. Margueritat, D. Machon, L. Saviot, F. Demoisson, and A. Mermet, Contact laws between nanoparticles: The elasticity of a nanopowder, *Nanoscale* **10**, 2154 (2018).

- [33] M. Hiraiwa, S. Wallen, and N. Boechler, Acoustic wave propagation in disordered microscale granular media under compression, *Granular Matter* **19**, 62 (2017).
- [34] G. Tas, J. Loomis, H. Maris, A. Bailes Iii, and L. Seiberling, Picosecond ultrasonics study of the modification of interfacial bonding by ion implantation, *Appl. Phys. Lett.* **72**, 2235 (1998).
- [35] T. Dehoux, O. B. Wright, R. Li Voti, and V. E. Gusev, Nanoscale mechanical contacts probed with ultrashort acoustic and thermal waves, *Phys. Rev. B* **80**, 235409 (2009).
- [36] T. Dehoux, O. B. Wright, and R. Li Voti, Picosecond time scale imaging of mechanical contacts, *Ultrasonics* **50**, 197 (2010).
- [37] M. Hettich, A. Bruchhausen, S. Riedel, T. Geldhauser, S. Verleger, D. Issenmann, O. Ristow, R. Chauhan, J. Dual, A. Erbe *et al.*, Modification of vibrational damping times in thin gold films by self-assembled molecular layers, *Appl. Phys. Lett.* **98**, 261908 (2011).
- [38] W. Ma, T. Miao, X. Zhang, M. Kohno, and Y. Takata, Comprehensive study of thermal transport and coherent acoustic-phonon wave propagation in thin metal film–substrate by applying picosecond laser pump–probe method, *J. Phys. Chem. C* **119**, 5152 (2015).
- [39] K. M. Hoogeboom-Pot, E. Turgut, J. N. Hernandez-Charpak, J. M. Shaw, H. C. Kapteyn, M. M. Murnane, and D. Nardi, Nondestructive measurement of the evolution of layer-specific mechanical properties in sub-10 nm bilayer films, *Nano Lett.* **16**, 4773 (2016).
- [40] M. Hettich, K. Jacob, O. Ristow, M. Schubert, A. Bruchhausen, V. Gusev, and T. Dekorsy, Viscoelastic properties and efficient acoustic damping in confined polymer nano-layers at GHz frequencies, *Sci. Rep.* **6**, 33471 (2016).
- [41] M. Grossmann, M. Schubert, C. He, D. Brick, E. Scheer, M. Hettich, V. Gusev, and T. Dekorsy, Characterization of thin-film adhesion and phonon lifetimes in Al/Si membranes by picosecond ultrasonics, *New J. Phys.* **19**, 053019 (2017).
- [42] J. D. Greener, E. de Lima Savi, A. V. Akimov, S. Raetz, Z. Kudrynskiy, Z. D. Kovalyuk, N. Chigarev, A. Kent, A. Patané, and V. Gusev, High-frequency elastic coupling at the interface of van der Waals nanolayers imaged by picosecond ultrasonics, *ACS Nano* **13**, 11530 (2019).
- [43] H. Zhang, A. Antoncicchi, S. Edward, I. Setija, P. Planken, and S. Witte, Unraveling Phononic, Optoacoustic, and Mechanical Properties of Metals with Light-Driven Hypersound, *Phys. Rev. Appl.* **13**, 014010 (2020).
- [44] C. Grünsteidl, I. Veres, T. Berer, S. Kreuzer, R. Rothmund, M. Hettich, E. Scherleitner, and M. Rzyzy, Measurement of the attenuation of elastic waves at GHz frequencies using resonant thickness modes, *Appl. Phys. Lett.* **117**, 164102 (2020).
- [45] G. V. Hartland, Optical studies of dynamics in noble metal nanostructures, *Chem. Rev.* **111**, 3858 (2011).
- [46] T. Devkota, B. S. Brown, G. Beane, K. Yu, and G. V. Hartland, Making waves: Radiation damping in metallic nanostructures, *J. Chem. Phys.* **151**, 080901 (2019).
- [47] P. Maioli, T. Stoll, H. E. Saucedo, I. Valencia, A. Demessence, F. Bertorelle, A. Crut, F. Vallee, I. L. Garzon, G. Cerullo *et al.*, Mechanical vibrations of atomically defined metal clusters: From nano- to molecular-size oscillators, *Nano Lett.* **18**, 6842 (2018).
- [48] T. Devkota, D. Chakraborty, K. Yu, G. Beane, J. E. Sader, and G. V. Hartland, On the measurement of relaxation times of acoustic vibrations in metal nanowires, *Phys. Chem. Chem. Phys.* **20**, 17687 (2018).
- [49] K. Bertoldi, D. Bigoni, and W. Drugan, Structural interfaces in linear elasticity. Part I: Nonlocality and gradient approximations, *J. Mech. Phys. Solids* **55**, 1 (2007).
- [50] G. Torrisi, E. Cavaliere, F. Banfi, G. Benetti, R. Raciti, L. Gavioli, and A. Terrasi, Ag cluster beam deposition for TCO/Ag/TCO multilayer, *Sol. Energy Mater. Sol. Cells* **199**, 114 (2019).
- [51] G. Benetti, E. Cavaliere, F. Banfi, and L. Gavioli, Antimicrobial nanostructured coatings: A gas phase deposition and magnetron sputtering perspective, *Materials* **13**, 784 (2020).
- [52] H. Ogi, N. Nakamura, and M. Hirao, Picosecond ultrasound spectroscopy for studying elastic modulus of thin films: A review, *Nondestructive Testing and Evaluation* **26**, 267 (2011).
- [53] D. Bigoni and A. Movchan, Statics and dynamics of structural interfaces in elasticity, *Int. J. Solids Struct.* **39**, 4843 (2002).
- [54] See Supplemental Material at <http://link.aps.org/supplemental/10.1103/PhysRevB.104.035416> for the parametric study for the pillar model (fixed q and low values of α).
- [55] F. Medeghini, A. Crut, M. Gandolfi, F. Rossella, P. Maioli, F. Vallée, F. Banfi, and N. Del Fatti, Controlling the quality factor of a single acoustic nanoresonator by tuning its morphology, *Nano Lett.* **18**, 5159 (2018).
- [56] K. Wegner, P. Piseri, H. V. Tafreshi, and P. Milani, Cluster beam deposition: A tool for nanoscale science and technology, *J. Phys. D* **39**, R439 (2006).
- [57] F. Bisio, M. Palombo, M. Prato, O. Cavalleri, E. Barborini, S. Vinati, M. Franchi, L. Mattered, and M. Canepa, Optical properties of cluster-assembled nanoporous gold films, *Phys. Rev. B* **80**, 205428 (2009).
- [58] F. Borghi, M. Milani, L. G. Bettini, A. Podestà, and P. Milani, Quantitative characterization of the interfacial morphology and bulk porosity of nanoporous cluster-assembled carbon thin films, *Appl. Surf. Sci.* **479**, 395 (2019).
- [59] B. Budiansky, On the elastic moduli of some heterogeneous materials, *J. Mech. Phys. Solids* **13**, 223 (1965).
- [60] See Supplemental Material at <http://link.aps.org/supplemental/10.1103/PhysRevB.104.035416> for the displacement field modulus for the first ($n = 0$) and the second ($n = 1$) film breathing modes for several α values.
- [61] See Supplemental Material at <http://link.aps.org/supplemental/10.1103/PhysRevB.104.035416> for the EMA model best fit solution for mode $n = 1$.
- [62] G. Benetti, E. Cavaliere, A. Canteri, G. Landini, G. M. Rossolini, L. Pallecchi, M. Chiodi, M. J. Van Bael, N. Winckelmans, S. Bals *et al.*, Direct synthesis of antimicrobial coatings based on tailored bi-elemental nanoparticles, *APL Mater.* **5**, 036105 (2017).
- [63] Z.-K. Kao, Y.-H. Hung, and Y.-C. Liao, Formation of conductive silver films via inkjet reaction system, *J. Mater. Chem.* **21**, 18799 (2011).
- [64] H. Peng, Y. Sripanich, I. Vasconcelos, and J. Trampert, Benchmarking wave equation solvers using interface

- conditions: The case of porous media, *Geophys. J. Int.* **224**, 355 (2020).
- [65] F. Vialla and N. Del Fatti, Time-domain investigations of coherent phonons in van der Waals thin films, *Nanomaterials* **10**, 2543 (2020).
- [66] J. Chaste, A. Missaoui, S. Huang, H. Henck, Z. Ben Aziza, L. Ferlazzo, C. Naylor, A. Balan, A. T. C. Johnson, R. Braive, and A. Ouerghi, Intrinsic properties of suspended MoS₂ on SiO₂/Si pillar arrays for nanomechanics and optics, *ACS Nano* **12**, 3235 (2018).
- [67] K. L. Johnson, K. Kendall, and A. D. Roberts, Surface energy and the contact of elastic solids, *Proc. R. Soc. London Ser. A* **324**, 301 (1971).
- [68] B. V. Derjaguin, V. M. Muller, and Y. P. Toporov, Effect of contact deformations on the adhesion of particles, *J. Colloid Interface Sci.* **53**, 314 (1975).
- [69] See Supplemental Material at <http://link.aps.org/supplemental/10.1103/PhysRevB.104.035416> for the parametric study for the computation of the surface energy and pull-off pressure.